

Supplemental material for: Two-dimensional melting under quenched disorder

July 30, 2013

1 Time-averaged orientational order

Fig. 4 of the main article shows the analysis for the experimental data. Figure 1 shows the same analysis performed for simulations. There is very good agreement between experiment and simulations.

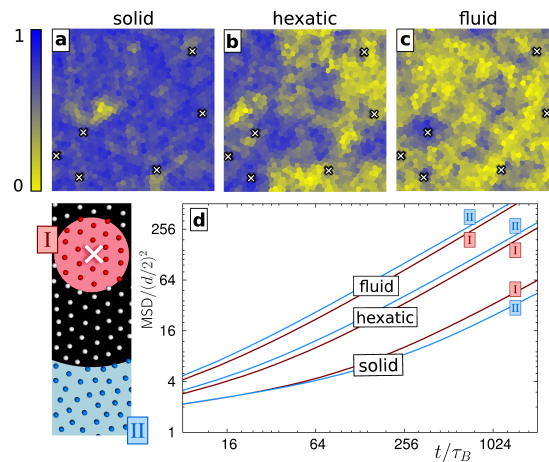


Figure 1: (a-c): Same as Figure 4 in the main paper but now for the simulations. Snapshots of the simulation system at 0.5% pinning, showing the local orientational order parameter $\langle |\psi_6| \rangle_t$ averaged over $\approx 70 \tau_B$ in the different phases (a: $\Gamma^{-1} = 0.01429$, b: $\Gamma^{-1} = 0.01471$, c: $\Gamma^{-1} = 0.01563$,). The field of view corresponds to $450\mu\text{m} \times 450\mu\text{m}$. Voronoi cells are color-coded according to the bar on the left. (d): Mean square displacement (MSD) calculated for particles within a distance of $8d$ around pinning sites (region I in inset) and more than $24d$ away from them (region II). The temperatures for solid, hexatic and fluid phase correspond to (a-c).

2 Description of the movies

To illustrate the fluctuations of the order parameter near the hexatic-isotropic liquid and hexatic-solid phase transition, we calculate the time evolution of the magnitude of the local bond order parameter $|\psi_6| = \left| \frac{1}{n_j} \sum_k e^{i6\theta_{jk}} \right|$ for both, experiment and simulation for long time runs. Like in Fig. 4, a-c in the main text and Fig. 1 of the supp. mat. particles are represented by their Voronoi cells and pinned sites are marked with crosses. The Voronoi cells are color-coded with the magnitude of the local bond-order parameter $\langle |\psi_6| \rangle_t$ averaged for a finite time window. This time window was chosen to be shorter than the orientational correlation time at the hexatic-isotropic liquid transition to analyze the present local order. This was repeated for a duration much longer than the orientational correlation time at the given temperature. A movie (with linear time scale) was constructed from the images. As can be seen in the movies for both, experiment and simulation, the local bond order field shows heterogeneities in space and time. This can be interpreted as critical(-like) fluctuations of the orientational order field. Patterns of similar magnitude do not persist in time as expected for systems with phase equilibria, nor do they move due to possible grain boundary dynamics. The patterns clearly emerge and disappear on various time and length scales, marking a continuous (or second order) phase transition. In addition, the fluctuations seem to be slightly enhanced in regions with increased pinning which might point to a dependency of critical fluctuations on quenched disorder.

- Movie 1: Experimental data recorded at $\Gamma^{-1} = 0.01447$ and 0.48% pinning, covering a time frame of $\approx 4080\tau_B \approx 8$ days. $\langle |\psi_6| \rangle_t$ was averaged over $\approx 42 \tau_B$.
- Movie 2: Simulation data recorded at $\Gamma^{-1} = 0.0146$ and 0.5% pinning, covering a time frame of $\approx 2700\tau_B$. $\langle |\psi_6| \rangle_t$ was averaged over $\approx 70 \tau_B$.

3 Polynomial fit criterion

In order to quantify the characteristic decay properties of $g_6(t)$ in the solid, hexatic and fluid phase, the linearly equidistant $g_6(t)$ data points are fitted with a second order polynomial fit on a double-logarithmic scale. This is achieved by calculating the least square parabola

$$\ln(g_6(t)) = a + b \ln(t/\tau_B) + c \ln^2(t/\tau_B) \quad (1)$$

with dimensionless coefficients a , b and c for the set of values $(\ln(t/\tau_B), \ln(g_6(t)))$. To characterize solid, hexatic and fluid phase, the relative contribution of curvature is considered, expressed by the ratio $c/|b|$. In the fluid phase, $g_6(t)$ decays exponentially, and the polynomial fit (1) exhibits negative curvature, $c/|b| < 0$. In the solid phase, $g_6(t)$ approaches a constant value such that the data is best approximated by a positively curved polynomial, $c/|b| > 0$. Since the algebraic decay of $g_6(t)$ corresponds to a linear decay in the log-log plot, the relative contribution of curvature vanishes, $c/|b| \approx 0$. We

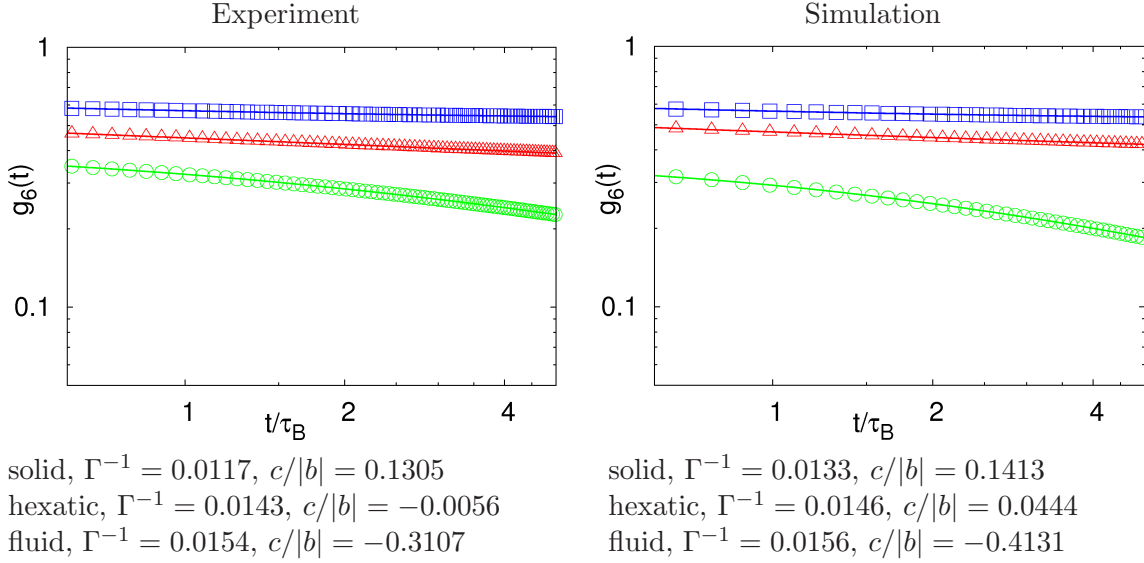


Figure 2: Exemplary $g_6(t)$ curves recorded in experiment & simulation (symbols) for the solid (blue squares), hexatic (red triangles) and isotropic fluid phase (green circles) fitted with the second order polynomial fit (1) (solid lines). The effective temperature Γ^{-1} and relative contribution of curvature $c/|b|$ are stated below the plot. The fraction of pinned particles is 0.48% in the experiment and 0.5% in the simulation.

define a lower and an upper threshold, $c/|b| = \pm 0.07$ to map all $g_6(t)$ curves recorded to the three phases (see Table 1).

| phase | $g_6(t)$ | $c/ b $ |
|---------|-------------------|------------------------------|
| solid | constant | > 0.07 |
| hexatic | algebraic decay | $-0.07 \leq c/ b \leq 0.07$ |
| fluid | exponential decay | < -0.07 |

Table 1: Characterization of solid, hexatic and fluid phase via the relative curvature contribution in Eq. (1).

For an equivalent treatment of experimental and simulation data, we consider the time-window $0.6 \leq t/\tau_B \leq 5$ and shift the origin to $t_0/\tau_B = 0.6$ to ensure $b < 0$, see Fig. 2. The phase diagram depicted in Fig. 3 of the main article is obtained with these settings. To test our approach for longer times, the polynomial fit is extended to $t/\tau_B = 400$ for the simulation data (Fig. 3), at which all properties of the phase diagram are recovered (see Fig. 4).

As a further consistency check, we applied the polynomial fit criterion to correlation

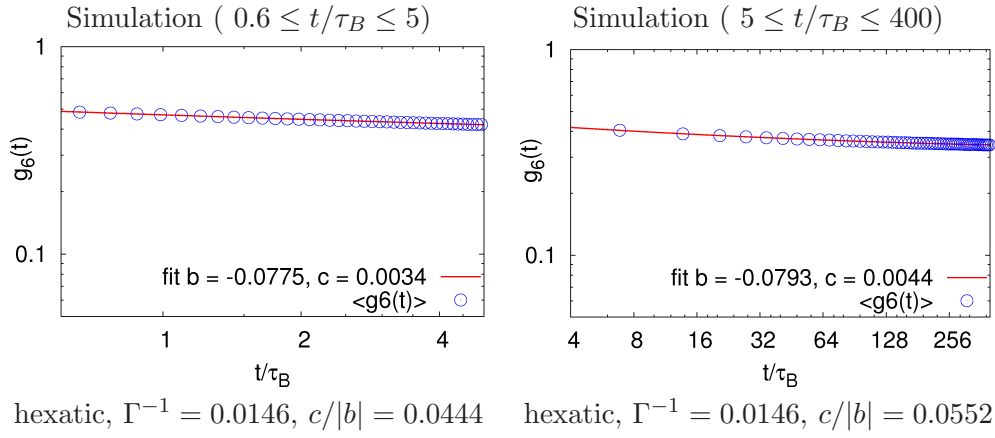


Figure 3: Second order polynomial fit applied to exemplary simulation data for times $0.6 \leq t/\tau_B \leq 5$ (left) and $5 \leq t/\tau_B \leq 400$ (right).

function data recorded in Ref. [1]. The envelope of the local maxima of $g_6(r)$ was fitted in the range $0.5 \leq r/\sigma \leq 64$. In doing so, our approach was found to recover the distinction drawn in [1] between curves corresponding to the fluid, hexatic and solid phase (see Fig. 1 therein).

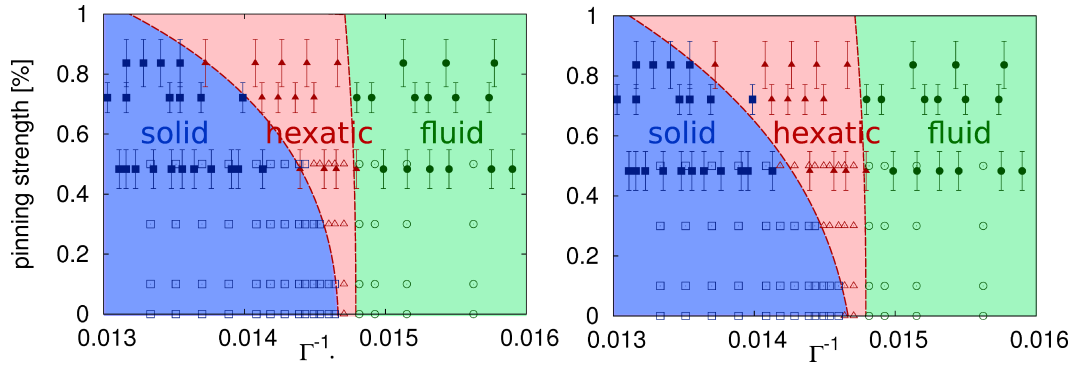


Figure 4: Phase diagram with simulation data fitted in the time-range $0.6 \leq t/\tau_B \leq 5$ (left) or $5 \leq t/\tau_B \leq 400$ (right). Open symbols represent simulation data, while full symbols correspond to experimental results. The latter are not altered and are shown for comparison only. The phase diagram does not change significantly if the parameters are varied, covering a large range of values.

[1] N. Gribova, A. Arnold, T. Schilling, and C. Holm, J. Chem. Phys. **135**, 054514 (2011).

4 Further evidence of the continuous nature of the melting process

A full cooling and heating cycle was conducted in the computer simulations. At each temperature step, the mean specific energy $\langle U \rangle$ was calculated. The results are depicted in Fig. 5. The cooling and heating branches collapse, which indicates a continuous phase transition. In order to distinguish between the observed widening of the hex-

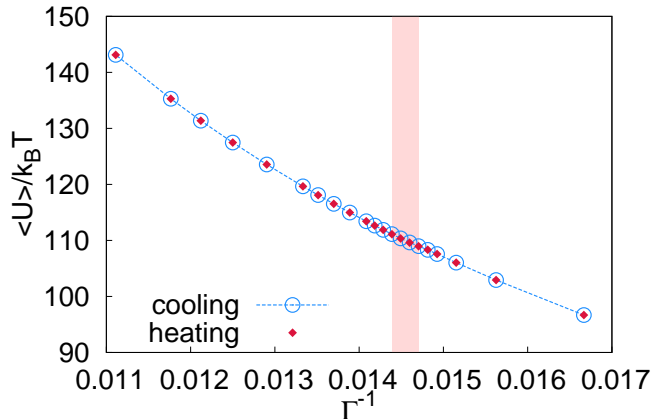


Figure 5: Mean specific energy $\langle U \rangle$ for cooling (open circles) and heating (full diamonds). The pinning fraction is 0.5%. The temperature range corresponding to the intermediate hexatic phase is indicated in red.

atic phase with increasing disorder and the signature of a polycrystalline structure, we examine a polycrystalline reference system by quenching an isotropic bulk fluid to the deep solid phase in the computer simulation. The resulting configuration consists of several crystalline regions with different orientations, which are sharply separated by grain boundaries, see Fig. 6. In comparison, a snapshot of the system with pinning in the hexatic phase exhibits no grain boundaries and apart from the spatio-temporal fluctuations discussed in the main article, there is globally homogeneous orientational order (Fig. 6). Furthermore, we monitor the probability distribution of the squared value of the orientational order parameter ψ_{6L} on various length scales. As discussed in [1], a monomodal distribution is expected in the absence of polycrystallinity. Our results are shown in Fig. 7 and clearly indicate a single peak in the distribution. While in the isotropic fluid phase, the distribution diverges at $\psi_{6L}^2 = 0$ (Fig. 7 (a)), the location of the peak shifts to intermediate values at the isotropic \rightarrow hexatic transition (b) and approaches higher values as the system is cooled further (c). For the pinning system, the distribution is clearly monomodal, while the distribution is bimodal for the polycrystalline reference system, see Fig. 7 (d).

To provide further evidence for the continuous nature of the phase transition, we conduct a finite-size scaling analysis of the fluctuation of the translational and orientational

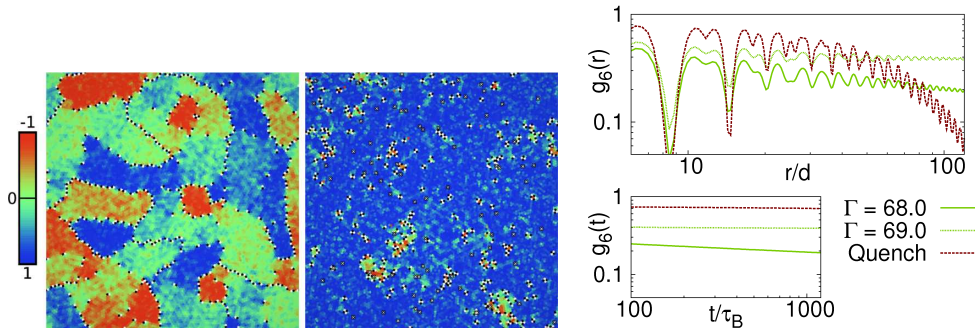


Figure 6: Left, Middle: Computer simulation snapshots showing the orientation of the local director $\psi_{6,i}$ relative to the global director ψ_6 . The colorcode corresponds to the bar on the left and is based on the normalized scalar product $\psi_{6,i} \cdot \psi_6 / (|\psi_{6,i}| |\psi_6|)$. Five- and sevenfolded defects are shown in black or white, respectively. Left: Pure bulk system after a quench from $\Gamma = 60$ to $\Gamma = 200$. Middle: System with 0.5% pinning in the hexatic phase ($\Gamma = 69.5$). Crosses indicate the positions of pinned particles. Right: Spatial and temporal correlation functions $g_6(r)$ (top) and $g_6(t)$ (bottom) calculated for the quenched polycrystalline system (red dashed curve). As a reference, typical computer simulation curves from the hexatic phase are shown for the system with 0.5% pinning (green solid / dotted curve).

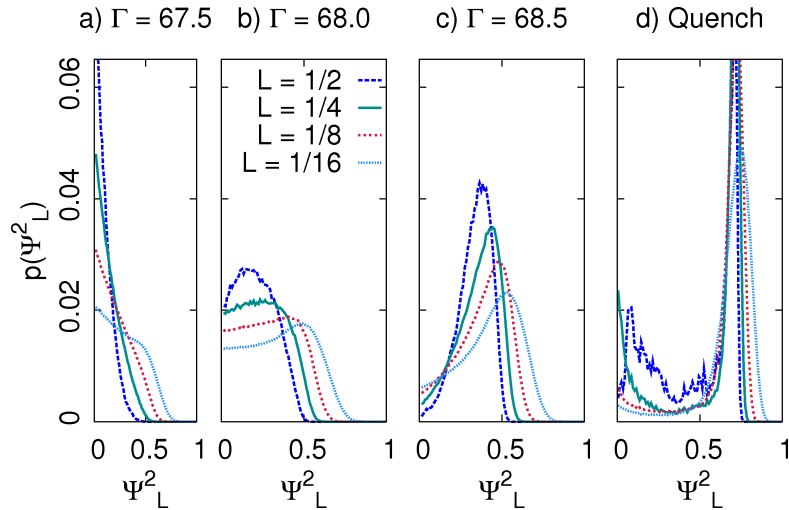


Figure 7: Probability distribution of Ψ_L^2 calculated for subcells of sidelength L (stated as a fraction of the total box length). (a-c) System with pinning, (d) Quenched polycrystalline configuration (shown in Fig. 6).

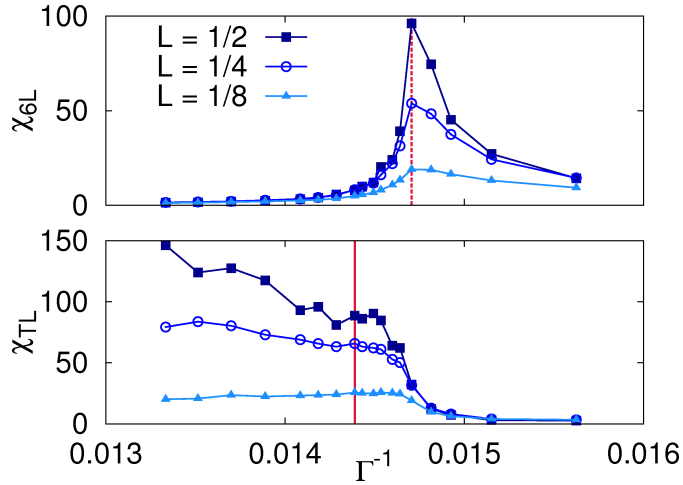


Figure 8: Top: Susceptibility χ_{6L} of the orientational order parameter as defined in [2] versus effective temperature calculated for subcells of sidelength L (stated as a fraction of the total box length). The dashed line corresponds to T_i derived from the analysis of $g_6(t)$. Bottom: Susceptibility χ_{TL} of the translational order parameter. The solid line corresponds to T_m derived from the analysis of $g_6(t)$. Data is shown for computer simulations, the pinning fraction is 0.5%.

order parameters ψ_T and ψ_6 , respectively. Therefore, we consider the translational and orientational susceptibilities χ_{TL} and χ_{6L} as defined in Ref. [2]. Our results are shown in Fig. 8. The susceptibility χ_{6L} diverges at the value of T_i estimated by the analysis of $g_6(t)$. At a lower temperature close to the estimated value of T_m , χ_{TL} undergoes a reasonable increase, then decreases for large systems once again pointing to a possible divergence for $L \rightarrow \infty$. The maximum in the susceptibility χ_{TL} occurs at higher coupling than that of χ_{6L} (for $L = 1/2$). The existence of two distinct temperatures for the divergent behavior of χ_{6L} and χ_{TL} indicates the two-step melting process. Further, it has to be pointed out that finding a proper reciprocal lattice vector \vec{G} is essential for a reliable analysis of the translational order parameter ψ_T , its correlation, and susceptibility. For statistically independent ensembles, \vec{G} will change and should be calculated separately for every ensemble. This has been done in our analysis, we determined the lattice vector that maximizes ψ_T for every ensemble. However, this becomes increasingly difficult approaching the hexatic phase due to the increasing dislocation densities. Furthermore, in the hexatic phase the reciprocal lattice vector is no longer defined since the translational order is short range and no lattice exists.

[2] Y. Han, N. Y. Ha, A. M. Alsayed, A. G. Yodh, Phys. Rev. E **77**, 041406 (2008).

5 Spatial correlation functions

In addition to the analysis of the temporal correlation function $g_6(t)$ stated in the main article, the spatial correlation function $g_6(r) = \langle \psi_6^*(r) \psi_6(0) \rangle$ is discussed here. Figure 5 shows exemplary curves for $g_6(r)$ in the isotropic fluid, hexatic and solid phase for experimental and simulation data. The decay behavior in the different phases is clearly distinguishable. While in the isotropic fluid $g_6(r)$ decays exponentially, it has an algebraic signature in the hexatic phase, and approaches a constant value in the solid, excluding the possibility of polycrystallinity. Consistent with Poisson statistics, there is an accumulation of pinned particles in the lower left corner of the experimental sample, see Fig. 10. This induces a small distortion of the lattice in the lower left corner leading to the weak decay of the experimental curve in the solid phase at $\Gamma = 119.5$. Since the orientational correlation in the time domain is robust to such distortions it is better suited to identify the transition temperature.

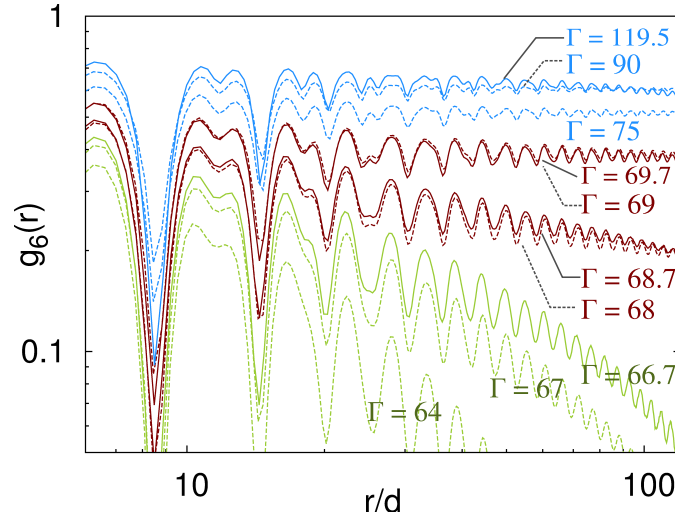


Figure 9: Spatial correlation function $g_6(r)$ of the bond order parameter in the presence of quenched disorder plotted versus reduced distance r/d on a double-logarithmic scale. The fraction of pinned particles is 0.48% in the experiment and 0.5% in the simulation. Exemplary curves are shown for the isotropic fluid (green), hexatic (red), and solid (blue) phase, where experimental data is drawn with solid, computer simulations with dashed lines.

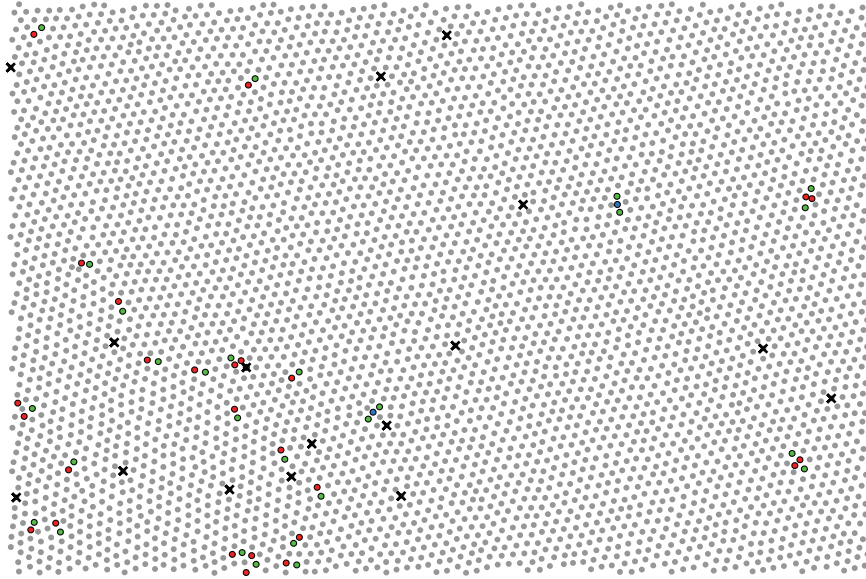


Figure 10: Snapshot of the system at $\Gamma = 119.5$ illustrating the defect distribution. Particles with six nearest neighbors are colored gray, fivefold coordinated sites red, sevenfold green, and particles with more than seven or less than 5 nearest neighbors are colored blue. Pinned particles are marked with crosses. The lower left of the field of view shows a small distortion due to an accumulation of pinned particles in the experiment.